PAPER

Check for updates

Synthesis and Brønsted acid doping of solution processable poly(thienylene vinylene) for thermoelectric application†

Wei-Ni Wu,‡[a] Kei-ichiro Sato,‡[b] Jun-Hao Fu,[c] Yi-Tsu Chan, [iD][c] Jhih-Min Lin,[d] Shih-Huang Tung, [iD][e] Tomoya Higashihara [iD] *[b] and Cheng-Liang Liu [iD] *[af]

Doped polythiophene (PT)-based semiconductors are of significant interest in the field of organic electronics, and are designed for novel thermoelectric applications based on their remarkable electrical properties, ease of processing, and tunable molecular structures. In the present study, the effects of the vinyl linkers in the PTs are systematically investigated in order to understand the interdependence of the structural properties, thin film morphologies, and thermoelectric performance. In particular, the soluble poly(thienylene vinylene) (PTV)-based conjugated polymer, poly[3,4-bis(2-ethylhexyl)thienylene vinylene] (P3,4EHTV), is synthesized *via* halogen-free and transition metal-free polymerization, and compared with the often-studied poly[3-(ethylhexyl)thiophene] (P3EHT) analogue. In addition, the thermoelectric properties of these two PT films doped with tris(pentafluorophenyl)borane ($B(C_6F_5)_3$, BCF) are characterized. Furthermore, the bipolaron states of the doped P3,4EHTV are retrieved *via* detailed ultra violet-visible-near infrared (UV-vis-NIR) and electron paramagnetic resonance (EPR) spectral analyses. Systematic microstructural characterizations reveal that the introduction of vinyl groups into the conjugated polymer backbone results in good miscibility with the BCF dopant, along with enhanced doping efficiency, thereby providing the appropriate sites for accommodating the dopant without disrupting the original chain packing and charge transport channels. The maximum power factor (PF) is measured as 1.47 $\mu W\ m^{-1}\ K^{-2}$ for the BCF-doped P3,4EHTV with a molar ratio of 20%, due to the high electrical conductivity (σ) of 0.34 S cm^{-1}, which is ten-fold higher than that of the P3EHT (0.17 $\mu W\ m^{-1}\ K^{-2}$). The present study therefore provides a suitable methodology for the realization of doped polymers with good host–dopant miscibility, compatible morphologies, and undisrupted microstructural packing in order to favor an increased power factor by introducing vinylene linkers into the main chains of PTs.

Introduction

In recent years, increasing demands for renewable energy *via* a green route have motivated researchers to seek innovative methods for enhancing the efficiency of conversion of heat energy to electricity. Traditionally, such thermoelectric effects

[a]*Department of Materials Science and Engineering, National Taiwan University, Taipei 10617, Taiwan. E-mail: liucl@ntu.edu.tw*

[b]*Department of Organic Materials Science, Graduate School of Organic Materials Science, Yamagata University, 4-3-16 Jonan, Yonezawa, Yamagata 992-8510, Japan. E-mail: thigashihara@yz.yamagata-u.ac.jp*

[c]*Department of Chemistry, National Taiwan University, Taipei 10617, Taiwan*

[d]*National Synchrotron Radiation Research Center, Hsinchu 30076, Taiwan*

[e]*Institute of Polymer Science and Engineering, National Taiwan University, Taipei 10617, Taiwan*

[f]*Advanced Research Center for Green Materials Science and Technology, National Taiwan University, Taipei 10617, Taiwan*

† Electronic supplementary information (ESI) available. See DOI: https://doi.org/10.1039/d3ta01117h

‡ These authors equally contribute to this work.

have been realized predominantly *via* inorganic materials, with the successful development of solid state devices for the applications of refrigeration and power generation. Although some inorganic alloy-based materials have exhibited relatively high thermoelectric performances, their applications are limited by the high costs of the raw materials and manufacturing facilities, as well as metal toxicity and poor processability.[1,2] By contrast, organic/polymeric materials possess facile solution processability, low cost, light weight, low thermal conductivity, and flexible form, all of which offer the potential for excellent thermoelectric performance, especially for low-grade waste heat harvesting.[3–8] The optimization of the molecular doping level of conjugated polymers is an effective approach to achieving a balance between the electrical conductivity (σ) and Seebeck coefficient (S) at the maximum power factor (PF).[9–13] However, only a few well-known conjugated polymers have been exploited in thermoelectric applications to-date,[14–16] with the most representative organic thermoelectric materials being the thiophene-based conjugated polymers. Hence, it can be anticipated that the recent increased interest in energy harvesting will

This journal is © The Royal Society of Chemistry 2023

J. Mater. Chem. A, 2023, 11, 17091–17100 | 17091

stimulate the rational design and synthesis of thermoelectric polythiophenes (PTs) with controlled molecular structures and doping processes. Within the PT-based thermoelectric family, the regioregular poly(3-hexylthiophene) (P3HT) has been mostly studied,[17,18] and P3HT films with high electrical conductivities can be achieved by exposing them to 2,3,5,6-tetrafluoro-7,7,8,8-tetracyanoquinodimethane (F4TCNQ) vapor.[19–21] However, this approach requires tedious sequential vapor doping rather than simple mixing of the F4TCNQ and polymer solution due to the limited solubility of F4TCNQ in the organic solvents that are commonly used to dissolve P3HT. Meanwhile, with the exception of oxidative doping, Lewis acid dopants such as ferric chloride ($FeCl_3$) provide an alternative approach for the doping of P3HT with high doping efficiency.[22–24] Unfortunately, however, the $FeCl_3$-doped conjugated polymers exhibit poor air stability, which needs to be overcome.

Tris(pentafluorophenyl)borane ((C_6F_5)$_3$B; BCF) has been considered as a promising p-type dopant due to its strong Lewis acidity and high solubility in organic solvents.[25–28] The doping principle relies on the interaction between the boron atom on BCF as the Lewis acid, and the conjugated polymer backbone as the Lewis base, which involves the redistribution of electron density and the formation of Lewis-acid adducts or charge transfer complexes (CTCs). Although these adducts and CTCs are harmful to the charge transfer ability, it has recently been reported that the BCF molecule is able to react with water to form a BCF-water complex, thereby inducing the Brønsted acid doping effect without forming adducts or CTCs.[29–32] In the absence of strong Lewis basic groups, BCF can hardly react with weak Lewis basic atoms and, hence, the doping mechanism based on the formation of the BCF-water complex is preferable. For instance, Suh *et al.* demonstrated BCF-doped P3HT thermoelectric materials[30] with high electrical conductivities and corresponding power factors of up to 28.3 μW m^{-1} K^{-2}. However, the applicability of BCF and its Brønsted acid effect for doping other PT-based thermoelectric derivatives have yet to be investigated.

Poly(thienylene vinylene)s (PTVs) are PT analogues with the addition of vinylene units between the thiophene rings along the main chain, and exhibit characteristic properties such as coplanar backbone structure,[33] low bandgap,[34] high thermal stability, and charge mobility.[33,35] Since PTV was first synthesized by polymerization based on the Wittig reaction in the 1970s,[36] versatile synthetic methods have been developed. Typically, PTVs can be synthesized by polymerization using transition-metal catalysts. For example, poly(3-hexylthienylene vinylene) has been synthesized by polycondensation based on the McMurry coupling reaction,[37] while poly(3-dodecylthienylene vinylene) was synthesized by polycondensation based on the Migita–Kosugi–Stille coupling reaction between 2,5-dibromo-3-dodecylthiophene and 1,2-bis(tributyltin)ethylene.[38] In addition, acyclic diene metathesis polymerization has been utilized for the synthesis of PTVs using symmetric 2,5-divinyl monomers and ruthenium catalysts.[39]

However, it has recently become preferable to avoid using transition-metal catalysts and halogen moieties[40–42] in the synthesis of semiconducting polymers due to their potential negative impact on the environment.[43,44] To this end, Horner–Wadsworth–Emmons (HWE) condensation reaction has been used for the transition-metal-free and halogen-free synthesis of PTVs.[45–47] For example, the present authors reported the controlled synthesis of poly[3-(2-ethylhexyl)thienylene vinylene] (P3EHTV) with predictable number-average molecular weights (M_n = 1800–10 200) and relatively low molar-mass dispersities ($Đ_M$ = 1.20–1.28) via the HWE polycondensation proceeding in a chain-growth manner.[47] However, due to the highly coplanar backbone and, hence, low solubility of the P3EHTV, it was difficult to obtain a high-molecular-weight sample (M_n > 11k) in this system. Hence, for facile device fabrication and evaluation, improvements in the molecular weights of the PTVs obtained via the HWE polymerization are important.

In this study, poly[3,4-di(2-ethylhexyl)thienylene vinylene] (P3,4EHTV) is first synthesized by the transition-metal-free and halogen-free HWE polycondensation of a newly-designed 3,4-dialkylated thiophene monomer with two 2-ethylhexyl groups. P3,4EHTV is shown to possess a high M_n of 31 400 with excellent solubility in organic solvents even in hexane. The effects of the vinylene linker in the PTs are then studied by comparing poly[3-(ethylhexyl)thiophene] (P3EHT) and P3,4EHTV, along with the corresponding BCF doping effects, via spectral, morphological, and microstructural analysis. Moreover, the correlation between the structures and thermoelectric properties of these two PT films with various molar ratios of BCF highlights the influence of the doping effect and dopant distribution in semicrystalline PT, which plays a crucial role in determining the thermoelectric performance.

Results and discussion

Synthesis and characterizations

As shown in Scheme 1a, double side chains composed of 2-ethylhexyl groups on a single thiophene ring were designed in a monomer precursor (**1a**) having active methylene phosphate and formyl moieties in order to improve the solubility of PTV. Further details are provided in the Synthesis section in ESI.† The synthesis of P3,4EHTV was achieved via the transition-
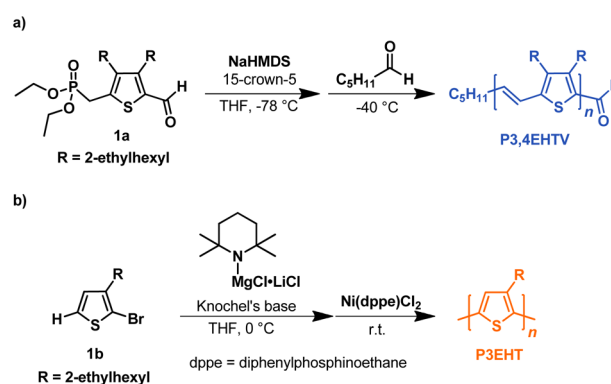
Scheme 1 Synthetic routes for (a) P3,4EHTV via the transition-metal-free and halogen-free Horner–Wadsworth–Emmons polycondensation, and (b) P3EHT via Kumada–Tamao catalyst transfer polycondensation using Knochel's base.

metal-free and halogen-free polycondensation based on the Horner–Wadsworth–Emmons reaction employing **1a**, following the previously-reported protocol with modification.[47] The polymerization of **1a** was initiated using hexanal in tetrahydrofuran (THF) at -78 °C in the presence of sodium bis(trimethylsilyl) amide (NaHMDS)/15-crown-5 as a base, and the reaction mixture was allowed to stand at -40 °C for 2 h (Scheme 1a). After the polymerization, the P3,4EHTV was purified by sequential Soxhlet extraction with methanol and acetone under a nitrogen atmosphere. Finally, hexane was used to collect the desired P3,4EHTV with a high M_n (SEC) of 31 400 and a $Đ_M$ of 2.09. For comparison, the regioregular poly[3-(2-ethylhexyl) thiophene] (P3EHT) (M_n (SEC) = 22 800, $Đ_M$ = 1.28, regioregularity = 99%) was synthesized by Kumada–Tamao catalyst transfer polycondensation using the Knochel's base according to the previously-reported procedure (Scheme 1b).[48] The ^{1}H or ^{13}C nuclear magnetic resonance (NMR) spectra for characterization of each monomer and the synthesized polymer are shown in Fig. S1–S7.† The molar-mass dispersities of P3,4EHTV measured from size exclusion chromatography are shown in Fig. S8.†

To the best of the present authors' knowledge, this is the first time to that an M_n greater than 30k has been achieved for poly(thieneylene vinylene) obtained *via* the transition-metal-free and halogen-free polycondensation based on the HWE reaction. This success is attributed to high solubility of P3,4EHTV in THF at -40 °C provided by the double branched side chains, which results in improved solubility of the growing polymer without precipitation during the polymerization. Based on the thermogravimetric analysis (TGA) in Fig. S9a,† P3,4EHTV exhibits good thermal stability, with a 5%-weight loss temperature ($T_d^{5\%}$) of 343 °C. Moreover, the phase transition behavior is revealed by the differential scanning calorimetry (DSC) results in Fig. S9b,† where the P3,4EHTV exhibits an endothermic peak in the second heating scan due to the melting temperature (T_m = 160 °C).

Spectroscopic studies

The optical properties of the as-synthesized polymers in diluted CHCl$_3$ solution and in the form of thin films are revealed by the UV-vis-near infrared (UV-vis-NIR) spectra in Fig. S10,† and their corresponding maximum absorption wavelengths (λ_{max}) and optical bandgaps (E_g) are summarized in Table 1. In the case of the P3EHT solution, a broad absorption with λ_{max} at 440 nm is observed, along with a low-intensity shoulder at 520 nm, while the thin film exhibits a significant red shift to λ_{max} = 495 nm, with the shoulder at 567 nm. However, the absorption spectrum of the P3,4EHTV exhibits a more obvious red shift, with a λ_{max} of 604 nm for the film compared to that of P3EHT film. In addition, P3,4EHTV solution spectrum exhibits a clear vibronic peak at 651 nm, assigned to 0–0 transition, indicative of strong pre-aggregation behavior due to the strong intermolecular interactions of polymer conjugated backbone stabilized by the vinylene unit. This is confirmed by the less pronounced red-shifted absorbance of thin film compared to the solution one. Meanwhile, the absorption band of P3,4EHTV becomes broader as compared with P3EHT due to an increase of degree of coplanarity of the conjugated backbone.[49,50] The additional vinylene unit in the main chain also causes the changes in the 0–0 and 0–1 transitions of the thin film absorption. An increase in the ratio of the absorption heights of the first two vibronic peaks (A_{0-0}/A_{0-1}) is also observed for the P3,4EHTV relative to the P3EHTV, indicating enhanced order within the polymer aggregates and increased conjugation length for the P3,4EHTV.[51] Further, the optical band gap (E_g^{opt}) of the P3,4EHTV to be determined as 1.77 eV from Tauc plot, which is lower than that of the P3EHT (2.04 eV) due to the incorporation of the vinylene unit into the polymer backbone.

The successful molecular doping and the extent of oxidation of the polymers with the addition of BCF are confirmed by the solution-state optical absorption spectra in Fig. S11,† and for the P3EHT and P3,4EHT films in Fig. 1a and b, respectively. As noted above, each polymer absorbs mainly in the visible region prior to doping. After doping, however, a dramatic bleaching of the polymer absorption is observed depending upon the dopant concentration, and is accompanied by the appearance of new (bi)polaronic bands in the NIR region. For example, in the case of the P3EHT film (Fig. 1a), the peak at 495 nm is seen to have decreased, but is not fully depleted, and two new absorption peaks have appeared at 800 nm and >1200 nm. Similarly, at a low doping concentration, the spectrum of the BCF-doped P3,4EHTV film shows the emergence of two new absorption features at 1290 nm and above 1900 nm (Fig. 1b) due to the generation of (bi)polarons as charge carriers. Moreover, as the doping concentration is increased to 40%, the intensities of the absorption bands above 1900 nm become higher than that of the peak at 1290 nm, thereby indicating that the polymer chains are fully oxidized.[52–54] Simultaneously, the neutral polymer absorption peak is almost fully depleted. In addition, the absorption maximum of the P3,4EHTV film is blue shifted from

Table 1 Fundamental properties of P3EHT and P3,4EHTV

| Sample | $M_n{}^a$ | $Đ_M{}^a$ | $T_d^{5\%\,b}$ (°C) | $T_m{}^c$ (°C) | $T_c{}^d$ (°C) | λ_{max} (nm) | | A_{0-0}/A_{0-1} | $E_g^{opt\,g}$ (eV) |
						Solution^e	Film^f		
P3,4EHTV	31 000	2.09	343	160	n.d.	651	604	0.85	1.77
P3EHT	22 800	1.21	427	n.d.	n.d.	440	495	0.59	2.04

^{a} Determined from SEC (eluent: THF at 40 °C, UV detector, λ = 254 nm, flow rate = 1.0 mL min^{-1}, polystyrene standard). ^{b} 5% weight loss temperature determined by TGA. ^{c} Melting temperature determined by DSC. ^{d} Crystallization temperature determined by DSC. ^{e} In CHCl$_3$ with concentration of $\sim$3 × 10^{-4} mM. ^{f} Drop-cast films on glass substrate. ^{g} Extracted from Tauc plot.

This journal is © The Royal Society of Chemistry 2023

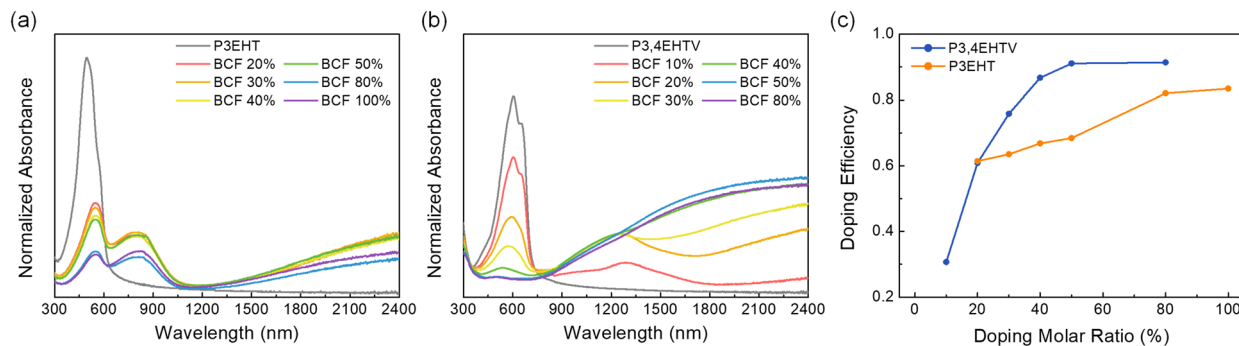*J. Mater. Chem. A*, 2023, **11**, 17091–17100 | **17093**

Fig. 1 (a and b) Thickness-normalized UV-vis-NIR absorption spectra of BCF-doped (a) P3EHT and (b) P3,4EHTV thin films. (c) Doping efficiencies of BCF-doped polymers as a function of doping molar ratio.

604 to 500 nm, and the (bi)polaronic absorption peak at 1290 nm is blue shifted to 1250 nm, with the increase in dopant concentration. This hypsochromic behavior further testifies to the formation of bipolarons.[55,56]

Due to the strong absorption overlap in the range of 750–2400 nm, it is difficult to evaluate the degrees of charge transfer for the polaron and bipolaron separately.[54] Therefore, instead of using the increased intensity for the (bi)polaron, the doping efficiency (η_{doping}) is calculated from the reduced intensity of the polymer absorption maximum upon doping[57] by using eqn (1):

$$\eta_{\text{doping}} = \frac{I_{\text{undoped}} - I_{\text{doped}}}{I_{\text{undoped}}} \quad (1)$$

where I_{pristine} is the λ_{max} intensity of the undoped polymer, and I_{doped} is the intrinsic absorption peak intensity of the doped polymer (for example, 547 nm for the 30% BCF-doped P3EHT film, and 595 nm for the 20% BCF-doped P3,4EHTV film). The doping efficiencies of P3EHT and P3,4EHTV films are plotted against the doping concentration in Fig. 1c. Here, the doping efficiency of P3EHT film is seen to increase moderately with the increase in doping concentration, whereas that of the P3,4EHTV film rapidly increases and then saturates at the doping concentration of 50%.

The ultraviolet photoelectron spectra (UPS) of the undoped and doped conjugated polymer films are provided in Fig. S12.† These are used to extract the work functions from the secondary electron cutoff (SECO) region, and to obtain the difference between the Fermi level and the highest occupied molecular orbital (HOMO) level from the onset position of the HOMO region. The HOMO levels of the undoped P3EHT and P3,4EHTV are −5.07 and −5.41 eV, respectively. The downshift of the HOMO energy level in the P3,4EHTV is probably due to the two bulky ethylhexyl side substituents,[58,59] despite the incorporation of the vinylene group into the PT backbone.[60,61] It has been reported that conjugated polymers with lower ionization potentials (shallower HOMO levels) possess stronger Lewis basic properties, thus providing them with the potential to generate Lewis acid-base complexes with a dopant.[62] Therefore, it is speculated that Lewis-acid doping of the P3EHT will be more favorable than that of the P3,4EHTV. Moreover, the increased

number of branched side chains on the P3,4EHTV may cause considerable steric hindrance and impede the binding between the sulfur atom of the thiophene with the boron atom of the BCF, thus hindering the formation of the Lewis acid-base adduct. Meanwhile, the effective p-doping of BCF into the polymers, along with the downshift of the Fermi level, are confirmed by a decrease in the work function from 3.40 to 4.17 eV for the P3EHT film, and from 3.93 to 4.46 eV for the P3,4EHTV film. Similarly, the binding energy of the onset position of the HOMO region decreases from 1.67 to 1.01 eV for P3EHT, and from 1.48 to 1.10 eV for P3,4EHTV, due to doping. The calculated HOMO levels of the undoped and 30%-doped P3EHT are −5.07 and −5.18 eV, respectively, while those of undoped and 20%-doped P3,4EHTV are −5.41 and −5.56 eV, respectively. Similar trends in the HOMO energy levels of the undoped and doped samples are derived from the photoelectron spectra in air (PESA), as shown in Fig. S13.†

The applicability of BCF as a p-type dopant in P3EHT and P3,4EHTV is further evaluated by the electron paramagnetic resonance (EPR) spectra of the undoped and doped polymer films in Fig. 2. Here, both undoped polymers appear spin-silent (*i.e.*, the EPR signals remain flat, thereby indicating the absence of single-spin polarons[30,63]). Meanwhile, the doped P3EHT solution exhibits a clear EPR signal centered at a g-factor of 2.003 shown in Fig. 2a, which becomes more intense as the doping concentration is increased from 20% to 100%. This indicates an increase in the number of polaron states as the doping level of P3EHT increases. For the doped P3,4EHTV as
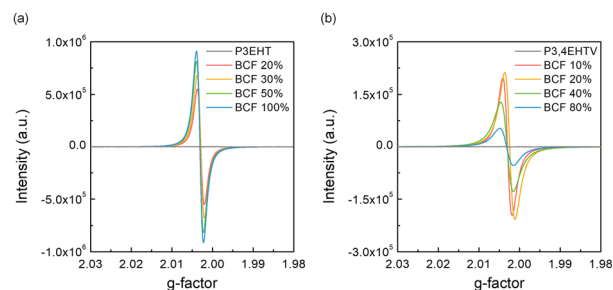

Fig. 2 EPR spectra of the undoped and various BCF-doped (a) P3EHT and (b) P3,4EHTV solutions.

shown in Fig. 2b, however, the EPR signal initially increases with the increase in doping concentration up to 20%, but then decreases with further doping due to the formation of undetectable polaron-pairs or spinless bipolarons.[63,64] These results are comparable to the previously-reported Brønsted doping effect, and also suggest that the BCF doping is more efficient in the P3,4EHTV.[30] Combined with the absorption spectra in Fig. 1b, these results suggest that the formation of bipolaron states is more likely for P3,4EHTV at doping concentrations above 40%.

The formation of the BCF-water complex is confirmed by the ^{19}F NMR spectra in Fig. S14.† Here, the ^{19}F NMR spectrum of the pure BCF exhibits three characteristic peaks at -128.1, -142.0, and -160.0 ppm, representing the *ortho*-, *para*-, and *meta*-fluorine resonances, respectively.[65,66] In the presence of water, BCF can react to form a BCF-water complex, in accordance with the equilibrium $BCF + xH_2O \rightleftharpoons BCF\text{-}(H_2O)_x$,[30,32] thus leading to an upfield-shift and increased intensity of these characteristic NMR peaks. After BCF-doping, three peaks appear at -136.6, -157.6, and -164.5 for the P3EHT (with 30% BCF), and at -136.8, -160.4, and -165.8 for the P3,4EHTV (with 20% BCF), thus confirming the formation of the BCF-water complex. Furthermore, the doped P3,4EHTV exhibits a more noticeable upfield shift compared to that of the doped P3EHT relative to pure BCF, thereby suggesting a more significant complexation between BCF and H_2O. This, in turn, suggests a Brønsted acid doping process for the P3,4EHTV sample.

Next, the changes in the conformation of the PT in response to the doping process are revealed by the Raman spectra of the undoped and doped P3EHT and P3,4EHTV thin films in Fig. 3. The specific Raman modes observed for each polymer in the region between 1200 and 1800 cm^{-1} are shown in Fig. S15.† The primary characteristic peaks relate to the movements of carbon atoms in the thiophene rings, involving atoms adjacent to the sulfur atom (C_α) and atoms bonded to another carbon atom (C_β). Thus, the neat P3EHT film exhibits Raman bands at ~1378 and 1455 cm^{-1} due to the symmetric C_β–C_β and C_α–C_β vibrations, respectively. Meanwhile, P3,4EHTV exhibits three

characteristic Raman peaks at 1293, 1388, and 1576 cm^{-1} due to the vinyl C–H bending, C_α–C_β stretching, and vinyl C=C stretching vibrations, respectively, of the polymer backbone.[67] No significant changes are observed in the shapes of the Raman spectra of both polymers with the increase in dopant concentration. Therefore, to examine the doping-induced changes in the conformation of each polymer chain, the shift in the ring skeleton C_α–C_β mode upon doping is treated as representative. This peak position and width indicate the degree of doping and the molecular ordering in the PT films, respectively. At the highest investigated concentration of BCF, the C_α–C_β peak of the doped P3EHT film exhibits a red shift of ~12 cm^{-1}, while the maximally-doped P3,4EHTV exhibits a blue shift of 6 cm^{-1}. This is diagnostic of the formation of polarons in the P3EHT and bipolarons in the P3,4EHTV upon BCF doping,[68,69] and is consistent with the EPR results in Fig. 2. In addition, the broadening of the C_α–C_β peak with increased doping concentration for both polymers indicates an increase in the disorder ad charge of the polymer chains.[70]

Morphology and microstructure of BCF-doped polymer films

The surface morphologies of the undoped and doped P3EHT and P3,4EHTV thin films are revealed by the atomic force microscopy (AFM) height images in Fig. 4. Here, the pristine P3EHT (Fig. 4a) and P3,4EHTV (Fig. 4b) exhibit nanofibril-like interconnecting networks with relatively low root-mean-square roughness (R_{RMS}) values of 0.69 and 0.55 nm, respectively. Meanwhile, the corresponding phase images in Fig. S17 and S19† exhibit fine textures with small phase differences and feature sizes of less than 10 nm. Upon doping at concentrations of 10 to 80%, all of the P3,4EHTV films exhibit smooth surfaces and small R_{RMS} values (Fig. 4b and S18†), thereby indicating that the microscale morphology is unaffected by the incorporation of the dopant. By contrast, the doped P3EHT films exhibit rougher surfaces, along with considerable granular agglomeration and R_{RMS} values that gradually increase with the doping concentration (Fig. 4a and S16†). These results indicate that the P3,4EHTV host sustains good miscibility and high
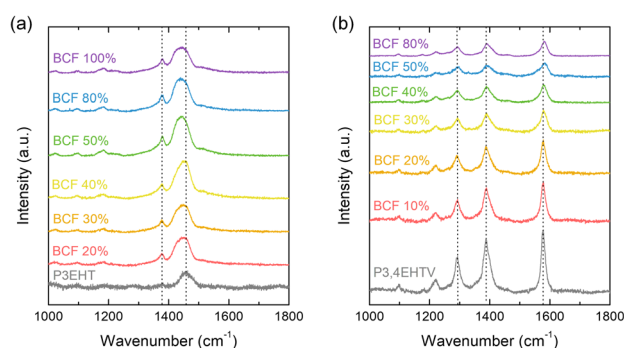

Fig. 3 Raman spectra of the undoped and various BCF-doped (a) P3EHT and (b) P3,4EHTV films. The peaks identified by the dotted lines are (from left to right) the C_α–C_β vibration and C_β–C_β vibration of the P3EHT, and the vinyl C–H vibration, C_α–C_β vibration and vinyl C=C vibration of the P3,4EHTV.
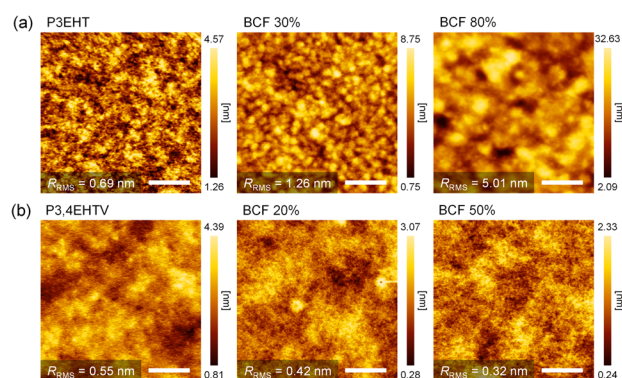

Fig. 4 AFM height images of (a) the undoped (left), 30%-BCF doped (middle), and 80%-BCF doped (right) P3EHT films, and (b) the undoped (left), 30%-BCF doped (middle), and 80%-BCF-doped (right) P3,4EHTV films (scale bar = 500 nm).

This journal is © The Royal Society of Chemistry 2023

J. Mater. Chem. A, 2023, **11**, 17091–17100 | **17095**

doping uniformity with the BCF dopant, whereas the P3EHT host does not.

The microstructural evolution of each polymer due to doping is further revealed by the 2D grazing-incidence wide-angle scattering (2D GIWAXS) patterns of the undoped and doped P3EHT in Fig. 5a and S20,† and those of the undoped and doped P3,4EHTV in Fig. 5b and S21.† The pristine P3EHT film exhibits high ordered (h00) Bragg peaks (up to (300) at $q = 0.42$, 0.85, and 1.28 Å^{-1}) are observed in both the in-plane and out-of-plane direction, indicating a (100) lamellar stacking of the alkylated side chains at a spacing of ∼15.0 Å. These results indicate the coexistence of mixed face-on and edge-on packing modes in the P3EHT. In addition, the diffraction peaks of (001) at $q = 0.63$ Å^{-1} and (010) at $q = 1.47$ Å^{-1} can be observed, with spacings of 10.0 and 4.3 Å along the ring and the interplanar direction, respectively, which is in agreement with previous reports.[71,72] By contrast, the less-ordered P3,4EHTV exhibits bimodal packing with only two (100) and (010) reflections at $q = 0.46$ and 1.40 Å^{-1}, corresponding to lamellar and interplanar spacings of 13.7 and 4.5 Å, respectively. This suggests that the rigid vinylene moieties in the P3,4EHTV backbone,[60,73] along with the bulky branched side chains[74] strongly impact upon the interchain interactions and alter the molecular ordering.

In each case, the effects of incorporating the BCF dopant into the polymer hosts can be seen in the corresponding GIWAXS patterns in Fig. 5a and b, and are further elucidated by the diffractogram profiles in Fig. 5c and d. Here, progressive changes are observed in the lamellar and interlayer spacings of each polymer as the amount of BCF doping is increased. In the case of the doped P3EHT film, the lamellar (100) peak at 0.42 Å^{-1} becomes broader, and a new peak indexed as (100)′ appears at ∼0.30 Å^{-1}, thus suggesting the formation of two crystalline textures. At the doping ratio of 30%, the (100)′ peak corresponds to a lamellar spacing of 20.7 Å, thereby indicating a highly expanded structure due to the intercalation of the dopant between the branched alkyl side chains of the P3EHT lattice (*i.e.*, type I molecular packing, which is commonly observed in doped polymers). Meanwhile, the lamellar spacing is reduced to

13.5 Å in the (100) direction and slightly increased to ∼4.4 Å in the (010) direction, thus suggesting a type II packing structure in which the dopant molecules are intercalated into the backbone interlayers. When the doping level is further increased, the most notable change is the complete disappearance of the (100)′ reflection, which indicates that the type II crystalline texture becomes dominant.

In addition, some diffraction spots are observed in the GIWAXS of P3EHT at the doping concentration of 80% (right-hand panel, Fig. 5a), which is probably due to the precipitation of BCF crystals in the presence of excess dopant. Taken together, these results suggest that the ordered packing of the P3EHT chains is highly disrupted upon doping due to the steric hindrance caused by the formation of charge transfer complexes (CTCs).[30] By comparison, the GIWAXS patterns of the BCF-doped P3,4EHTV films indicate little impact upon the crystal lattice along the side chains and π-conjugated inter-layers, with spacings of ∼14.0 and ∼4.5 Å, respectively, for all doping concentrations (Fig. 5b and d). Nevertheless, a new sharp diffraction peak is observed at $q_z = 0.49$ Å^{-1} at the BCF loading of 80% (Fig. S21†), which is consistent to the BCF pattern in Fig. S22,† thereby indicating the formation of BCF crystals. The largely unchanged lattice parameters can be attributed to the fact that the less-ordered regions of P3,4EHTV are able to accommodate the extrinsic dopants without dis-turbing the existing microstructural packing,[64,75,76] thereby achieving host/guest (conjugated polymer/BCF) miscibility. This is further verified by the diiodomethane contact angle measurements in Fig. S23.†[77,78] Here, the contact angle of the BCF is 46.6°, the contact angles of the pristine and 30% BCF-doped P3EHT samples are 62.5° and 52.3°, respectively, and the contact angles of the pristine and 20% BCF-doped P3,4EHTV are 60.5° and 50.6°, respectively. The smaller difference between the contact angles of the BCF dopant and the P3,4EHTV clearly demonstrates the better dopant/P3,4EHTV miscibility. This enhanced doping efficiency significantly facilitates the doping process, as observed in the UV-vis-NIR spectra (Fig. 1b) and AFM images (Fig. 4b).
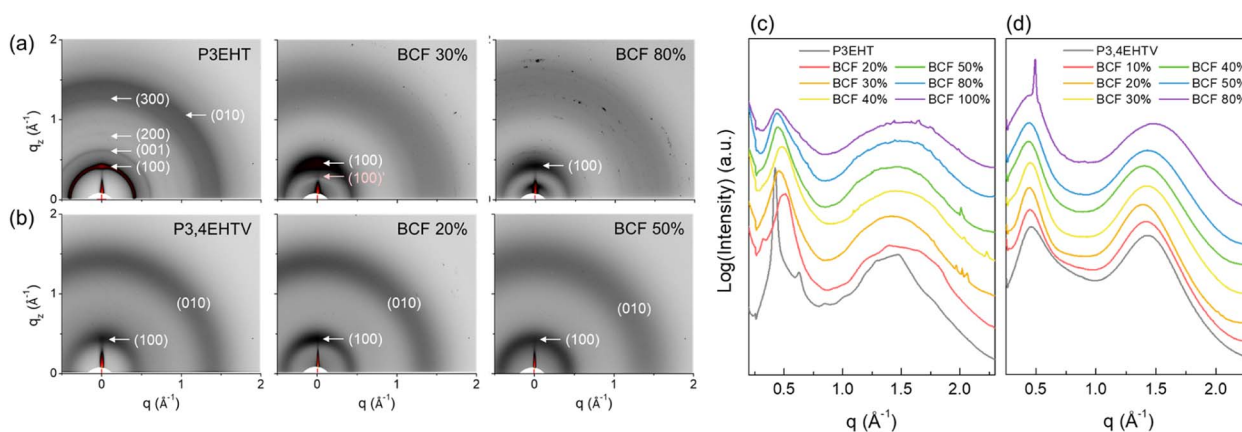

Fig. 5　(a and b) 2D GIWAXS patterns of (a) the undoped and BCF-doped P3EHT, and (b) the undoped and BCF-doped P3,4EHTV films; (c and d) the corresponding 1D line profiles.

Thermoelectric properties of BCF-doped polymer films

Since obtaining thermal conductivity of organic polymer thin film is challenging due to measurement deviation, the effects of the various BCF doping levels upon the thermoelectric performances of the P3EHT and P3,4EHTV polymer films are evaluated according to the power factor, which is obtained from eqn (2).

$$PF = S^2\sigma \qquad (2)$$

The measured thermoelectric properties are plotted in Fig. 6 and summarized in Table S1.† Thus, while both undoped polymers exhibit no electrical conductivity, the addition of BCF leads to a clear increase in this parameter up to a maximum value (σ_{max}) of 0.34 S cm^{-1} for the P3,4EHTV film doped with 20% BCF. Notably, this is five times higher than that of 30%-BCF doped P3EHT film. This significant enhancement is attributed to the better miscibility between P3,4EHTV and BCF, which prevents the disturbance of the molecular ordering (as demonstrated by the above microstructural analysis), thereby leading to better doping efficiency and an efficient charge transport pathway. However, further doping of the P3,4EHTV film causes a subsequent reduction in the electrical conductivity by two orders of magnitude. This is attributed to the escalating number of bipolarons, as indicated by the above spectroscopic analysis, which disfavor the hopping of charge carriers due to electrostatic repulsion.[79]

Meanwhile, the Seebeck coefficient of the P3,4EHTV film is seen to decrease from 344.3 ± 21.6 to 42.4 ± 11.9 μV K^{-1} as the level of BCF doping is increased from 10% to 80%, whereas that of the P3EHT only slightly decreases to 168.8 ± 22.6 μV K^{-1} at 100% doping. The positive Seebeck coefficients indicate that the BCF dopants preferentially extract electrons from the oxidized PTs, with hole transport mainly contributing to the conducting channel, while the gradual decrease in the Seebeck coefficient is attributed to an inverse relationship with the doping level. Furthermore, the noticeable reduction in the Seebeck coefficient of the doped P3,4EHTV film relative to that of the P3EHT film is attributed to the higher doping efficiency of the P3,4EHTV, as demonstrated by the absorption spectroscopy results. Consequently, the power factor follows the trend in the electrical conductivity, giving optimized values of 0.17 and 1.47 μW m^{-1} K^{-2} for the 30%-BCF doped P3EHT and the 20%-BCF doped P3,4EHTV, respectively. The ten times higher power factor of the optimally-doped P3,4EHTV film relative to the optimally-doped P3EHT film is attributed to the introduction of the vinylene group into the polymer backbone, which allows the doping to significantly enhance the electrical conductivity without greatly sacrificing the Seebeck coefficient. Fig. S24† displays the thermoelectric properties of the optimized doping condition at different temperatures, with measurements taken between 300 and 320 K to prevent de-doping at higher temperature. The electrical conductivity of 20% BCF-doped P3,4EHTV increases from 0.35 to 0.4 S cm^{-1}, while the increase of 30% BCF-doped P3EHT is slight, going from 0.057 to 0.067 S cm^{-1}. The enhancement of electrical conductivity is attributed to thermal-activated charge transport. The Seebeck coefficient for each polymer remains relatively constant over the measured temperature range. The temperature dependences of electrical conductivity and Seebeck coefficient are characteristic of hopping transport, which is commonly observed in organic semiconducting polymers.[80–82]

The charge transport mechanism of the BCF-doped polymer and the effects of introducing the vinylene group are further clarified by the temperature-dependent electrical conductivity measurements of the optimally-doped polymers in Fig. S25a.† Here, the electrical conductivity is seen to increase as the temperature is increased, and is well-fitted with the Arrhenius formula, eqn (3):

$$\sigma = \sigma_0 \exp\left(-\frac{E_A}{k_B T}\right) \qquad (3)$$

where σ_0 is the pre-exponential factor (here we use electrical conductivity measured at room temperature (303 K)), E_A is the activation energy, k_B is Boltzmann's constant, and T is temperature. This goodness of fit indicates a nearest-neighbor hopping transport process. The calculated activation energies of the optimally-doped P3EHT and P3,4EHTV are 134.9 and 103.9 meV, respectively. The weaker dependence of the as-doped P3,4EHTV indicates that it has a lower charge barrier due to the better miscibility with BCF and, hence, less disrupted molecular ordering, thus leading to a higher electrical conductivity and power factor.
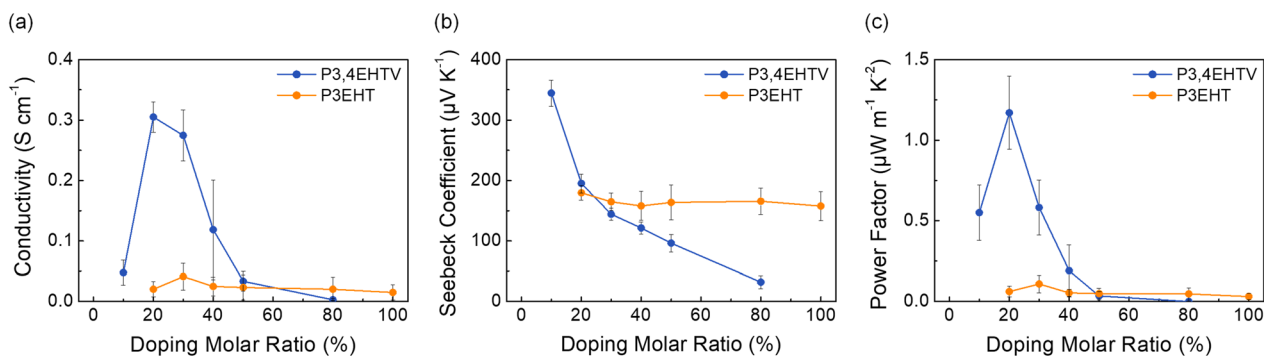

Fig. 6 The thermoelectric properties of the BCF-doped P3EHT and P3,4EHTV thin films as a function of doping molar ratio: (a) the electrical conductivity, (b) the Seebeck coefficient, and (c) the power factor.

This journal is © The Royal Society of Chemistry 2023

J. Mater. Chem. A, 2023, **11**, 17091–17100 | **17097**

In addition, Chabinyc *et al.* proposed the empirical correlation between the Seebeck coefficient and electrical conductivity of a polymer film given by eqn (4):[83]

$$S = \frac{k_B}{q}\left(\frac{\sigma}{\sigma_\alpha}\right)^{-1/4} \qquad (4)$$

where σ_α is the unclarified conductivity constant, which is fitted to be approximately 0.44 and 4.9 S cm^{-1}, and q is the unit charge. To compare the thermoelectric performances of the variously-doped P3EHT and P3,4EHTV films, the power law-dependent S–σ correlations with an exponent of −1/4 are plotted as solid black lines in Fig. S25b,† along with three power factor values ranging from 0.01 to 0.1 and 1 μW m^{-1} K^{-2}. Here, both doped polymer films exhibit a scaling law dependence at low BCF doping concentrations and a departure at high doping concentrations. The scatter of S–σ data points between the polymer films at low and high BCF doping concentrations reflects the increase in structural diversity and energetic disorder with the increase in doping concentration.[32]

In order to demonstrate the effect of increased molecular weight on the thermoelectric properties of P3,4EHTV, we conducted a doping test and fabricated a thermoelectric device using P3EHTV. Although P3EHTV has poor solubility and precipitates on the tube wall in chloroform (Fig. S26a†), we still conducted the doping test and confirmed it through UV-vis-NIR absorption spectra (Fig. S26b†). Upon doping, the polymer aggregation peak at 570 nm is gradually depleted, along with (bi)polaron peaks appearing at 1230 nm and above 1800 nm. The thermoelectric devices were fabricated using the same processing conditions and the electrical conductivity, Seebeck coefficient, and power factor were measured as presented in Fig. S27.† The electrical conductivity of P3EHTV initially increases and peaks at 0.10 S cm^{-1} with a 30% doping molar ratio, but then decreases with further doping. Meanwhile, the Seebeck coefficient decreases from 189.4 to 47.4 μV K^{-1} as the doping level increases from 10% to 100%. As a result, the optimized power factor is determined to be 0.024 m^{-1} K^{-2} for the 20%-BCF doped P3EHTV. These findings provide strong evidence for the optimized chemical structure of P3,4EHTV with an additional side chain, as well as the impact of molecular weight and solubility on doping and the thermoelectric properties.

Experimental section

Device fabrication and measurements

The conjugated polymers (10 mg mL^{-1}) were dissolved in chloroform, and heated at 50 °C for 30 min to enable complete dissolution. A solution of the BCF dopant (30 or 50 mg mL^{-1}) in chloroform was then added to each polymer solution to achieve dopant concentrations of 10–100% (in terms of the molar ratio of dopant molecules to polymer repeating units). The resulting mixture was heated at 50 °C for at least 10 min until the solution changed color, and was then vigorously stirred by using a vortex to ensure that the polymers and dopants were well mixed, and to assist the considerable interaction between them. Each doping solution (50 μL) was then drop-cast onto pre-cleaned

glass substrates (15 mm × 7.5 mm), and the thin films were annealed at 50 °C for 2 h in air to remove the residual solvent and to induce the formation of BCF-water complex. In addition, thin films of each polymer in the absence of a dopant were prepared using the same approach for comparison. The resulting film thicknesses were measured using a profilometer (Alpha-Step D-300, KLA), and were found to range from 2 to 6 μm. Silver paste contacts were then painted on both short sides of each substrate, and the Seebeck coefficient, electrical conductivity, and power factor were measured using an in-plane thin film thermoelectric measurement system (ZEM-3 M8 equipped with a high-resistance (∼10^7 Ω) kit; ADVANCE RIKO). In addition, the thermoelectric data were collected at 303 K under a low-pressure helium atmosphere. The Seebeck coefficient was estimated from the slope of the linear fit of the thermovoltage (ΔV) *vs.* temperature difference (ΔT) (*i.e.*, $S = \Delta V/\Delta T$). Three ΔT values (set to 20, 30, and 40 K) were imposed on the samples. At least five data points for each thermoelectric device were collected to obtain the average thermoelectric properties.

Conclusions

Herein, a soluble poly(thienylene vinylene) (PTV)-based polymer, namely poly[3,4-bis(2-ethylhexyl)thienylene vinylene] (P3,4EHTV) featuring vinyl linkers in the polythiophene (PT) chain was synthesized. In addition, the effects of doping with various concentrations of tris(pentafluorophenyl)borane (BCF) were investigated by examining the resulting thin film morphologies/microstructures and thermoelectric properties. The results indicated a decrease in the bandgap and increase in the power factor (PF) in the P3,4EHTV compared to the poly[3-(ethylhexyl)thiophene] (P3EHT) reference polymer. Due to the low ionization potential of the P3EHT, the generation of Lewis-acid/base charge transfer complexes (CTCs) upon doping resulted in a low doping efficiency and, hence, a considerable disruption of the molecular packing, as evidenced by the grazing-incidence wide-angle scattering (GIWAXS) results. This resulted in comparatively poor electrical conductivity and a correspondingly low power factor. By contrast, P3,4EHT exhibited a Brønsted acid doping effect, along with a high host-dopant miscibility and a less ordered microstructure that was not much altered by doping, thereby yielding the highest electrical conductivity and power factor of 0.34 S cm^{-1} and 1.47 μW m^{-1} K^{-2} at a BCF molar ratio of 20%. In our study, we elucidate the relationship between varied chemical structure of PT and thermoelectric properties upon doping with BCF. The results of the present work further emphasize the importance of vinyl linkers attached to the PT backbone for thermoelectric applications.

Author contributions

Wei-Ni Wu: conceptualization, methodology, device fabrication, data collection and characterization, writing – original draft, review and editing. Kei-ichiro Sato: methodology, synthesis, data collection and analysis. Jun-Hao Fu: data collection and analysis of ^{19}F NMR spectra. Yi-Tsu Chan: analysis of ^{19}F NMR spectra. Jhih-Min Lin: characterization of microstructures. Shih-Huang

17098 | *J. Mater. Chem. A*, 2023, **11**, 17091–17100

This journal is © The Royal Society of Chemistry 2023

Tung: supervision, methodology, characterization of microstructures. Tomoya Higashihara: supervision, methodology, funding acquisition, project administration, writing – original draft (synthetic section). Cheng-Liang Liu: supervision, funding acquisition, project administration, writing – review and editing.

Conflicts of interest

There is no conflict to declare.

Acknowledgements

References

1 B. Russ, A. Glaudell, J. J. Urban, M. L. Chabinyc and R. A. Segalman, *Nat. Rev. Mater.*, 2016, **1**, 16050.

2 Y. Zhang, Q. Zhang and G. Chen, *Carbon Energy*, 2020, **2**, 408–436.

3 C.-J. Yao, H.-L. Zhang and Q. Zhang, *Polymers*, 2019, **11**, 107.

4 M. Massetti, F. Jiao, A. J. Ferguson, D. Zhao, K. Wijeratne, A. Würger, J. L. Blackburn, X. Crispin and S. Fabiano, *Chem. Rev.*, 2021, **121**, 12465–12547.

5 L. Zhang, X.-L. Shi, Y.-L. Yang and Z.-G. Chen, *Mater. Today*, 2021, **46**, 62–108.

6 L. Deng and G. Chen, *Nano Energy*, 2021, **80**, 105448.

7 L. Deng, Y. Liu, Y. Zhang, S. Wang and P. Gao, *Adv. Funct. Mater.*, 2023, **33**, 2210770.

8 T. Cao, X.-L. Shi and Z.-G. Chen, *Prog. Mater. Sci.*, 2023, **131**, 101003.

9 Y. Lu, J.-Y. Wang and J. Pei, *Chem. Mater.*, 2019, **31**, 6412–6423.

10 W. Zhao, J. Ding, Y. Zou, C.-a. Di and D. Zhu, *Chem. Soc. Rev.*, 2020, **49**, 7210–7228.

11 T. L. D. Tam and J. Xu, *J. Mater. Chem. A*, 2021, **9**, 5149–5163.

12 A. D. Scaccabarozzi, A. Basu, F. Aniés, J. Liu, O. Zapata-Arteaga, R. Warren, Y. Firdaus, M. I. Nugraha, Y. Lin, M. Campoy-Quiles, N. Koch, C. Müller, L. Tsetseris, M. Heeney and T. D. Anthopoulos, *Chem. Rev.*, 2022, **122**, 4420–4492.

13 A. Tripathi, Y. Lee, S. Lee and H. Y. Woo, *J. Mater. Chem. C*, 2022, **10**, 6114–6140.

14 Z. Fan and J. Ouyang, *Adv. Electron. Mater.*, 2019, **5**, 1800769.

15 M. Lindorf, K. A. Mazzio, J. Pflaum, K. Nielsch, W. Brütting and M. Albrecht, *J. Mater. Chem. A*, 2020, **8**, 7495–7507.

16 S. Wang, G. Zuo, J. Kim and H. Sirringhaus, *Prog. Polym. Sci.*, 2022, **129**, 101548.

17 R. Kroon, D. A. Mengistie, D. Kiefer, J. Hynynen, J. D. Ryan, L. Yu and C. Müller, *Chem. Soc. Rev.*, 2016, **45**, 6147–6164.

18 F. Zhang and C.-a. Di, *Chem. Mater.*, 2020, **32**, 2688–2702.

19 E. Lim, K. A. Peterson, G. M. Su and M. L. Chabinyc, *Chem. Mater.*, 2018, **30**, 998–1010.

20 J. Hynynen, D. Kiefer and C. Müller, *RSC Adv.*, 2018, **8**, 1593–1599.

21 M. T. Fontana, D. A. Stanfield, D. T. Scholes, K. J. Winchell, S. H. Tolbert and B. J. Schwartz, *J. Phys. Chem. C*, 2019, **123**, 22711–22724.

22 C. T. Hong, Y. Yoo, Y. H. Kang, J. Ryu, S. Y. Cho and K.-S. Jang, *RSC Adv.*, 2015, **5**, 11385–11391.

23 Z. Liang, Y. Zhang, M. Souri, X. Luo, A. M. Boehm, R. Li, Y. Zhang, T. Wang, D.-Y. Kim, J. Mei, S. R. Marder and K. R. Graham, *J. Mater. Chem. A*, 2018, **6**, 16495–16505.

24 L. Wu, H. Li, H. Chai, Q. Xu, Y. Chen and L. Chen, *ACS Appl. Electron. Mater.*, 2021, **3**, 1252–1259.

25 P. Pingel, M. Arvind, L. Kölln, R. Steyrleuthner, F. Krafft, J. Behrends, S. Janietz and D. Neher, *Adv. Electron. Mater.*, 2016, **2**, 1600204.

26 B. Yurash, D. Leifert, G. N. M. Reddy, D. X. Cao, S. Biberger, V. V. Brus, M. Seifrid, P. J. Santiago, A. Köhler, B. F. Chmelka, G. C. Bazan and T.-Q. Nguyen, *Chem. Mater.*, 2019, **31**, 6715–6725.

27 Y. J. Jeong, J. Jung, E. H. Suh, D.-J. Yun, J. G. Oh and J. Jang, *Adv. Funct. Mater.*, 2020, **30**, 1905809.

28 K. A. Peterson and M. L. Chabinyc, *J. Mater. Chem. C*, 2022, **10**, 6287–6295.

29 B. Yurash, D. X. Cao, V. V. Brus, D. Leifert, M. Wang, A. Dixon, M. Seifrid, A. E. Mansour, D. Lungwitz, T. Liu, P. J. Santiago, K. R. Graham, N. Koch, G. C. Bazan and T.-Q. Nguyen, *Nat. Mater.*, 2019, **18**, 1327–1334.

30 E. H. Suh, J. G. Oh, J. Jung, S. H. Noh, T. S. Lee and J. Jang, *Adv. Energy Mater.*, 2020, **10**, 2002521.

31 M. Arvind, C. E. Tait, M. Guerrini, J. Krumland, A. M. Valencia, C. Cocchi, A. E. Mansour, N. Koch, S. Barlow, S. R. Marder, J. Behrends and D. Neher, *J. Phys. Chem. B*, 2020, **124**, 7694–7708.

32 E. H. Suh, S. B. Kim, H. S. Yang and J. Jang, *Adv. Funct. Mater.*, 2022, **32**, 2207413.

33 R. Kroon, M. Lenes, J. C. Hummelen, P. W. M. Blom and B. de Boer, *Polym. Rev.*, 2008, **48**, 531–582.

34 H. Eckhardt, L. W. Shacklette, K. Y. Jen and R. L. Elsenbaumer, *J. Chem. Phys.*, 1989, **91**, 1303–1315.

35 H. E. A. Huitema, G. H. Gelinck, J. B. P. H. van der Putten, K. E. Kuijk, C. M. Hart, E. Cantatore, P. T. Herwig, A. J. J. van Breemen and D. M. de Leeuw, *Nature*, 2001, **414**, 599.

36 V. G. Kossmehl, M. Härtel and G. Manecke, *Makromol. Chem.*, 1970, **131**, 37–54.

37 R. Toyoshima, K. Akagi and H. Shirakawa, *Synth. Met.*, 1997, **84**, 431–432.

This journal is © The Royal Society of Chemistry 2023

J. Mater. Chem. A, 2023, **11**, 17091–17100 | **17099**

38 R. S. Loewe and R. D. McCullough, *Chem. Mater.*, 2000, **12**, 3214–3221.

39 Y. Qin and M. A. Hillmyer, *Macromolecules*, 2009, **42**, 6429–6432.

40 G. Zhang, Y. Dai, Y. Liu, J. Liu, H. Lu, L. Qiu and K. Cho, *Polym. Chem.*, 2017, **8**, 3448–3456.

41 A. Onwubiko, W. Yue, C. Jellett, M. Xiao, H.-Y. Chen, M. K. Ravva, D. A. Hanifi, A.-C. Knall, B. Purushothaman, M. Nikolka, J.-C. Flores, A. Salleo, J.-L. Bredas, H. Sirringhaus, P. Hayoz and I. McCulloch, *Nat. Commun.*, 2018, **9**, 416.

42 L. Giraud, S. Grelier, E. Grau, G. Hadziioannou, C. Brochon, H. Cramail and E. Cloutet, *J. Mater. Chem. C*, 2020, **8**, 9792–9810.

43 Ö. Usluer, M. Abbas, G. Wantz, L. Vignau, L. Hirsch, E. Grana, C. Brochon, E. Cloutet and G. Hadziioannou, *ACS Macro Lett.*, 2014, **3**, 1134–1138.

44 J. Kuwabara, T. Yasuda, N. Takase and T. Kanbara, *ACS Appl. Mater. Interfaces*, 2016, **8**, 1752–1758.

45 C. Zhang, J. Sun, R. Li, S.-S. Sun, E. Lafalce and X. Jiang, *Macromolecules*, 2011, **44**, 6389–6396.

46 J. Sun, C. Zhang, S. Venkatesan, R. Li, S.-S. Sun and Q. Qiao, *J. Polym. Sci., Part B: Polym. Phys.*, 2012, **50**, 917–922.

47 E. Goto, Y. Ochiai, M. Ueda and T. Higashihara, *Polym. Chem.*, 2018, **9**, 1996–2001.

48 P.-S. Lin, Y. Shoji, S. N. Afraj, M. Ueda, C.-H. Lin, S. Inagaki, T. Endo, S.-H. Tung, M.-C. Chen, C.-L. Liu and T. Higashihara, *ACS Appl. Mater. Interfaces*, 2021, **13**, 31898–31909.

49 J. C. Speros, H. Martinez, B. D. Paulsen, S. P. White, A. D. Bonifas, P. C. Goff, C. D. Frisbie and M. A. Hillmyer, *Macromolecules*, 2013, **46**, 5184–5194.

50 Z. Zhang and Y. Qin, *Macromolecules*, 2016, **49**, 3318–3327.

51 F. C. Spano and C. Silva, *Annu. Rev. Phys. Chem.*, 2014, **65**, 477–500.

52 N. Massonnet, A. Carella, O. Jaudouin, P. Rannou, G. Laval, C. Celle and J.-P. Simonato, *J. Mater. Chem. C*, 2014, **2**, 1278–1283.

53 C. Enengl, S. Enengl, S. Pluczyk, M. Havlicek, M. Lapkowski, H. Neugebauer and E. Ehrenfreund, *ChemPhysChem*, 2016, **17**, 3836–3844.

54 I. Zozoulenko, A. Singh, S. K. Singh, V. Gueskine, X. Crispin and M. Berggren, *ACS Appl. Polym. Mater.*, 2019, **1**, 83–94.

55 B. D. Naab, X. Gu, T. Kurosawa, J. W. F. To, A. Salleo and Z. Bao, *Adv. Electron. Mater.*, 2016, **2**, 1600004.

56 X. Yan, M. Xiong, J.-T. Li, S. Zhang, Z. Ahmad, Y. Lu, Z.-Y. Wang, Z.-F. Yao, J.-Y. Wang, X. Gu and T. Lei, *J. Am. Chem. Soc.*, 2019, **141**, 20215–20221.

57 X.-Y. Wang, Y. Liu, Z.-Y. Wang, Y. Lu, Z.-F. Yao, Y.-F. Ding, Z.-D. Yu, J.-Y. Wang and J. Pei, *J. Polym. Sci.*, 2022, **60**, 538–547.

58 B. Burkhart, P. P. Khlyabich and B. C. Thompson, *Macromolecules*, 2012, **45**, 3740–3748.

59 J.-Y. Chu, C.-Y. Lin, T.-H. Tu, S.-H. Hong, Y.-Y. Chang, C.-W. Yang, Y.-T. Chan, C.-L. Liu, P. V. Komarov and S.-H. Tung, *Macromolecules*, 2021, **54**, 3689–3699.

60 L. Zhang, B. D. Rose, Y. Liu, M. M. Nahid, E. Gann, J. Ly, W. Zhao, S. J. Rosa, T. P. Russell, A. Facchetti, C. R. McNeill, J.-L. Brédas and A. L. Briseno, *Chem. Mater.*, 2016, **28**, 8580–8590.

61 S. H. Yu, K. H. Park, Y.-H. Kim, D. S. Chung and S.-K. Kwon, *Macromolecules*, 2017, **50**, 4227–4234.

62 C. C. Han and R. L. Elsenbaumer, *Synth. Met.*, 1989, **30**, 123–131.

63 F. Genoud, M. Guglielmi, M. Nechtschein, E. Genies and M. Salmon, *Phys. Rev. Lett.*, 1985, **55**, 118–121.

64 C.-Y. Yang, W.-L. Jin, J. Wang, Y.-F. Ding, S. Nong, K. Shi, Y. Lu, Y.-Z. Dai, F.-D. Zhuang, T. Lei, C.-A. Di, D. Zhu, J.-Y. Wang and J. Pei, *Adv. Mater.*, 2018, **30**, 1802850.

65 C. Bergquist, B. M. Bridgewater, C. J. Harlan, J. R. Norton, R. A. Friesner and G. Parkin, *J. Am. Chem. Soc.*, 2000, **122**, 10581–10590.

66 T. Beringhelli, D. Maggioni and G. D'Alfonso, *Organometallics*, 2001, **20**, 4927–4938.

67 J. Gao, A. K. Thomas, J. Yang, C. Aldaz, G. Yang, Y. Qin and J. K. Grey, *J. Phys. Chem. C*, 2015, **119**, 8980–8990.

68 J. Yamamoto and Y. Furukawa, *J. Phys. Chem. B*, 2015, **119**, 4788–4794.

69 A. E. Mansour, A. M. Valencia, D. Lungwitz, B. Wegner, N. Tanaka, Y. Shoji, T. Fukushima, A. Opitz, C. Cocchi and N. Koch, *Phys. Chem. Chem. Phys.*, 2022, **24**, 3109–3118.

70 J. Nightingale, J. Wade, D. Moia, J. Nelson and J.-S. Kim, *J. Phys. Chem. C*, 2018, **122**, 29129–29140.

71 B. W. Boudouris, V. Ho, L. H. Jimison, M. F. Toney, A. Salleo and R. A. Segalman, *Macromolecules*, 2011, **44**, 6653–6658.

72 L. Yu, E. Davidson, A. Sharma, M. R. Andersson, R. Segalman and C. Müller, *Chem. Mater.*, 2017, **29**, 5654–5662.

73 J.-J. Park, Y.-A. Kim, S.-H. Lee, J. Kim, Y. Kim, D.-H. Lim and D.-Y. Kim, *ACS Appl. Polym. Mater.*, 2019, **1**, 27–35.

74 B. Fu, J. Baltazar, A. R. Sankar, P.-H. Chu, S. Zhang, D. M. Collard and E. Reichmanis, *Adv. Funct. Mater.*, 2014, **24**, 3734–3744.

75 S. E. Yoon, Y. Kang, S. Y. Noh, J. Park, S. Y. Lee, J. Park, D. W. Lee, D. R. Whang, T. Kim, G.-H. Kim, H. Seo, B.-G. Kim and J. H. Kim, *ACS Appl. Mater. Interfaces*, 2020, **12**, 1151–1158.

76 J. Duan, J. Ding, D. Wang, X. Zhu, J. Chen, G. Zhu, C. Chen, Y. Yu, H. Liao, Z. Li, C.-a. Di and W. Yue, *Adv. Sci.*, 2023, **10**, 2204872.

77 J. Guo, K. Hu, B. Qiu, J. Zhang, D. Yang, L. Zhou, S. Li, L. Meng, Z. Zhang and Y. Li, *ACS Appl. Mater. Interfaces*, 2021, **13**, 36033–36043.

78 D. Rosas Villalva, S. Singh, L. A. Galuska, A. Sharma, J. Han, J. Liu, M. A. Haque, S. Jang, A. H. Emwas, L. J. A. Koster, X. Gu, B. C. Schroeder and D. Baran, *Mater. Horiz.*, 2022, **9**, 500–508.

79 D. Tsokkou, P. Cavassin, G. Rebetez and N. Banerji, *Mater. Horiz.*, 2022, **9**, 482–491.

80 J. Wu, Y. Sun, W.-B. Pei, L. Huang, W. Xu and Q. Zhang, *Synth. Met.*, 2014, **196**, 173–177.

81 H. Li, E. Plunkett, Z. Cai, B. Qiu, T. Wei, H. Chen, S. M. Thon, D. H. Reich, L. Chen and H. E. Katz, *Adv. Electron. Mater.*, 2019, **5**, 1800618.

82 S. A. Gregory, J. F. Ponder Jr, S. L. Pittelli, M. D. Losego, J. R. Reynolds and S. K. Yee, *ACS Appl. Polym. Mater.*, 2021, **3**, 2316–2324.

83 A. M. Glaudell, J. E. Cochran, S. N. Patel and M. L. Chabinyc, *Adv. Energy Mater.*, 2015, **5**, 1401072.

17100 | *J. Mater. Chem. A*, 2023, **11**, 17091–17100

This journal is © The Royal Society of Chemistry 2023